Integration of advanced 3D SPECT modelling for pinhole collimators into the open-source STIR framework

Matthew Strugari [1,2,*], Carles Falcon [3], Kjell Erlandsson [4], Brian Hutton [4], Kimberly Brewer [1,2,5], and Kris Thielemans [4]

[1] *Biomedical MRI Research Laboratory, Halifax, Canada*
[2] *Department of Physics and Atmospheric Science, Dalhousie University, Halifax, Canada*
[3] *Neuroimaging Group, Barcelonaβeta Brain Research Center, Barcelona, Spain*
[4] *Institute of Nuclear Medicine, University College London, London, UK*
[5] *Department of Diagnostic Radiology, Dalhousie University, Halifax, Canada*

Correspondence*:
Matthew Strugari
matthew.strugari@dal.ca

ABSTRACT

Pinhole-SPECT systems are becoming increasingly important in clinical and preclinical nuclear medicine investigations as they can provide a superior resolution-sensitivity tradeoff compared to conventional parallel-hole and fan-beam collimators. Previously, open-source software did not exist for reconstructing tomographic images from pinhole-SPECT datasets. A 3D SPECT system matrix modelling library specific for pinhole collimators has recently been integrated into STIR — an open-source software package for tomographic image reconstruction. The pinhole-SPECT library enables corrections for attenuation and the spatially variant collimator-detector response by incorporating their effects into the system matrix. Attenuation corrections can be calculated with a simple single line-of-response or a full model. The spatially variant collimator-detector response can be modelled with point spread function and depth of interaction corrections for increased system matrix accuracy. Improvements to computational speed and memory requirements can be made with image masking. This work demonstrates the flexibility and accuracy of STIR's forthcoming support for pinhole-SPECT datasets using measured and simulated single-pinhole SPECT data from which reconstructed images were analyzed quantitatively and qualitatively. The extension of the open-source STIR project with advanced pinhole-SPECT modelling will enable the research community to study the impact of pinhole collimators in several SPECT imaging scenarios and with different scanners.

Keywords: Image reconstruction, molecular imaging, Monte Carlo methods, nuclear medicine, SPECT

1 INTRODUCTION

Single-photon emission computed tomography (SPECT) is based on the detection of individual γ-rays emitted from a radiotracer distribution within a subject. An Anger camera detects the γ-rays with a scintillating crystal and associated electronics after they have passed through a collimator. The collimator acts as a lens to form a 2D projection image identifying the direction from which the γ-rays originated, and a series of projection images acquired from different angles can be subsequently used to reconstruct the 3D radiotracer distribution in a tomographic image.

The design of the collimator in terms of hole-size, material, and overall geometry, among other factors, affects the spatial resolution and sensitivity of a SPECT system. A number of designs exist including but not limited to parallel-hole, fan-beam, converging and diverging, slit-slat, coded-aperture, and single- and multi-pinhole collimators. Therefore, the choice of collimator design is application dependent in order to channel photons of different energies, magnify or minify images, or select between imaging quality and imaging speed **?**. Although parallel-hole and fan-beam collimators are conventionally used when imaging small fields-of-view (FOVs), pinhole collimators can provide a superior resolution-sensitivity tradeoff **??**. Besides the successful application of pinhole-SPECT systems in small-animal imaging, there has been a resurgence in the use of pinhole collimators for clinical cardiac and brain studies and when imaging small FOVs **?**.

While the use of pinhole-SPECT has regained popularity in clinical and preclinical investigations of molecular imaging agents, there are no open-source software solutions available for reconstructing pinhole-SPECT datasets. However, recent efforts have led to the integration of a 3D SPECT system matrix modelling library for pinhole collimators into the open-source Software for Tomographic Image Reconstruction (STIR). The STIR package is an object-oriented library implemented in C++ that provides a framework for research in the processing and reconstruction of emission tomography studies **?**. Initially written for support of positron emission tomography (PET) data, STIR was previously extended to handle SPECT data with parallel- and converging-hole collimators **??**. The expansion of STIR's support for pinhole collimators marks the first open-source platform for reconstructing pinhole-SPECT datasets which is important in the advancement of molecular imaging techniques and technologies.

This work aims to demonstrate the forthcoming capabilities of STIR's support for pinhole-SPECT datasets. This was achieved by integrating parts of the SPECT Reconstruction Library developed at the University of Barcelona (SRL-UB) into STIR **?**. The library enables corrections for the spatially variant collimator-detector response and attenuation by incorporating their effects into the system matrix.

2 TECHNICAL DESCRIPTION

Similar to the original `SPECTUB` implementation, the new pinhole-SPECT implementation is referred to as `PinholeSPECTUB` and includes a dedicated reader for SPECT projection data in interfile format **?**. The pinhole-SPECT interfile reader utilizes the projection matrix size, pixel scaling factor, and detector radius according to the face of the scintillating crystal. Calculation of the system matrix is executed with the `ProjMatrixByBinPinholeSPECTUB` projector class derived from the existing STIR `ProjMatrixByBin` class which utilizes a detector and collimator text file in addition to the usual STIR parameter file. The parameter file is a text file which uses an Interfile-like syntax. It is composed of keywords corresponding to the names of the various reconstruction and matrix parameters with the values entered next to them. A detailed description of all parameters can be found in STIR's documentation.

The detector file defines the intrinsic resolution for point spread function (PSF) corrections, scintillating crystal attributes for depth of interaction (DOI) corrections, and orbit information for the acquisition (i.e., initial angle, number of angles, angular increment, direction of rotation, and axial position with respect to the reconstructed volume). Note that only circular camera orbits are supported at this time. The collimator file defines the radius of rotation and geometry for cylindrical or polygonal collimators (i.e., the detector element exposed by the pinhole, hole position, shape, size, tilt, and acceptance angle). An illustration of the pinhole-SPECT system matrix geometry is shown in Fig. 2.

Figure 2 goes here.

The system matrix weights the contribution of each image voxel along the line of response (LOR) to each detector element. For increased system matrix accuracy, corrections can be made for the spatially variant collimator-detector response function in terms of intrinsic PSF, DOI, and/or attenuation (ATT) corrections by setting the appropriate fields in the parameter file. When PSF correction is disabled, a geometrical approach is applied by considering the shadow projection of the pinhole on the detector for higher computational speed and reduced memory requirements compared to the PSF approach, but is less accurate. When PSF correction is enabled, the shadow of the hole is convolved with the PSF in detector space to account for blurring effects of the camera. Values parsed from the parameter file define the number of sigmas to consider in the PSF along with the subsampling factor to temporally reduce PSF resolution for increased calculation accuracy before downsampling the final PSF to the bin size. Furthermore, when PSF or DOI corrections are enabled, an additional parsed parameter sets the spatial resolution in which to sample PSF and DOI distributions.

Enabling DOI corrections subdivides the scintillating crystal using Bresenham's line algorithm to correct for the crystal attenuation, and hence the DOI, along the LOR. If DOI correction is disabled, then the detector radius is taken to be the center of the scintillator. When ATT correction is enabled, a simple correction can be applied where the same attenuation factor is applied for the whole PSF, or a full correction can be applied where different attenuation factors are applied for each bin of the PSF **?**. Further improvements to speed and memory can be made with image masking using the default cylinder, an attenuation map, or a mask file. The default cylinder is based on the object radius in the image volume. It is important to always set the object radius greater than or equal to the size of the object in the attenuation map or mask file when masking as the matrix weights are calculated according to this value, and failure to do so will result in an error. The projection matrix can be kept in memory or calculated per projection angle. In the latter case, the memory is released before starting calculations on a new angle, thereby reducing memory requirements but increasing computation time for iterative reconstruction algorithms.

3 MATERIALS AND METHODS

To test the pinhole-SPECT implementation in STIR, Cubresa's novel silicon-photomultiplier (SiPM)-based preclinical SPECT system — The Spark — was used with the single-pinhole (SPH) collimator (Cubresa Inc., Winnipeg, Canada). This system was recently characterized with the National Electrical Manufacturers Association (NEMA) NU 1-2018 Standards for Performance Measurements of Gamma Cameras, and a corresponding Geant4 Application for Tomographic Emission (GATE) Monte Carlo model was validated **?**.

Simulations and image reconstructions were performed on an HP Z820 workstation operating Ubuntu 18.04.5 LTS with two Intel Xeon E5-2630 2.3 GHz hexa-core CPUs and 64 GB of 1600 MHz DDR3 memory. The SPH-SPECT data for quantitative image assessment was simulated with GATE v9.0 while qualitative image assessment was done with *in vivo* data. Tomographic images were reconstructed with STIR v5.0.2 on a single CPU core as the `PinholeSPECTUB` library has not yet been configured to use the Message Passing Interface capabilities of STIR which would allow it to perform several computations in parallel.

3.1 Quantitative assessment of reconstructed data

3.1.1 Phantom simulations and data generation

Phantom data was simulated with three different subjects containing technetium-99m (^{99m}Tc): a NEMA Micro-PET IQ phantom, a mouse-sized NEMA triple line source scatter phantom, and a volumetric cylinder. The IQ phantom (outer diameter $\varnothing_{\mathrm{OD}}$ = 33.5 mm, length L = 63.0 mm) was made from polymethyl methacrylate (PMMA) with three different regions of interest (ROIs): a spillover ROI with water and air, a uniform ROI (inner diameter $\varnothing_{\mathrm{ID}}$ = 30.0 mm, L = 15.0 mm), and an ROI with five hot rods ($\varnothing_{\mathrm{ID}} = \{1, 2, 3, 4, 5\}$ mm, L = 20.0 mm). The triple line source scatter phantom ($\varnothing_{\mathrm{OD}}$ = 25.4 mm, L = 60.0 mm) was made from acrylic housing three precision capillary tubes ($\varnothing_{\mathrm{OD}}$ = 0.8 mm, $\varnothing_{\mathrm{ID}}$ = 0.4 mm) with one located at the center and two with a 10.0 mm radial offset separated by 90 deg. The volumetric cylinder ($\varnothing_{\mathrm{OD}}$ = 28.0 mm, L = 55.0 mm) was made from acrylic with a uniform ROI of radioactivity ($\varnothing_{\mathrm{ID}}$ = 26.0 mm, L = 21.0 mm).

Table 1 summarizes the simulated phantom acquisitions, projection and reconstruction matrices, reconstruction algorithms, and applied analysis which are further described in the proceeding subsections. Note that the Spark has a fixed rotation extent of 270 deg and NEMA's specification of a 3 deg angular increment was used unless stated otherwise. GATE simulation results were output to Rapid Object-Oriented Technology (ROOT) format and subsequently converted to Cubresa's list mode format. Projection data with 0.5 mm bins were generated from list mode data using a 30%-wide energy window centered at 140 keV. Projection images were converted from Cubresa's format to Interfile format for use with STIR. Various reconstruction algorithms and matrix corrections were then used to assess figures of merit in terms of computation cost, contrast-to-noise ratio, resolution, uniformity, and variability.

Table 1. Summary of simulated phantom acquisitions and reconstructions.

Subject	Activity	Acquisition	Projections	Projection matrix	Reconstruction matrix	Algorithm[1]	Analysis[2]
IQ phantom	50 MBq	Forward proj.	64 (8 subsets)	104×104 px, 1.0 mm	120×92×92 vx, 0.5 mm	OSEM	Computation cost
		3600 s	91 (7 subsets)	208×208 px, 0.5 mm	230×184×184 vx, 0.25 mm	OSEM, OSOSL, OSSPS	Hot rod CNR
Line source	30 MBq	5460 s	91 (7 subsets)	208×208 px, 0.5 mm	230×184×184 vx, 0.25 mm	OSEM	Resolution
Cylinder	20 MBq	910 s	91 (7 subsets)	208×208 px, 0.5 mm	230×184×184 vx, 0.25 mm	OSEM	Uniformity & CV

[1] OSEM: Ordered subsets expectation maximization, OSOSL: Ordered subsets one step late with median root prior (penalization factor, PF = 1.0), OSSPS: Ordered subsets separable paraboloidal surrogate with quadratic prior (PF = 0.3).

[2] CNR: Contrast-to-noise ratio, CV: Coefficient of variation.

3.1.2 Computation cost with different matrix corrections

To compare computation costs for different types of matrix corrections and masking, a forward projection of the IQ phantom was made with 64 views over 360 deg (see Table 1). Memory requirements and CPU time when storing the matrix in memory were compared to calculating it per projection angle. The maximum RAM and CPU time were recorded with Ubuntu's `/usr/bin/time -v` command when calling STIR's `OSMAPOSL` program from the command line. The ordered subset expectation maximization (OSEM) algorithm was used with 8 subsets and 40 subiterations, and the matrix was calculated with no corrections (N-C), attenuation correction (ATT-C), DOI correction (DOI-C), PSF correction (PSF-C), all corrections (ATTDOIPSF-C), and all corrections with masking (ATTDOIPSFM-C) using the default cylindrical mask ($\varnothing$ = 34.0 mm) **?**.

3.1.3 Contrast-to-noise ratios in the IQ phantom

A sample sinogram of the hot rods is shown in Fig. **??** where Fig **??** is the GATE result and Fig. **??** is the forward projected STIR result including attenuation, PSF, and DOI effects. Visual agreement between these sinograms suggests that

To compare different reconstruction algorithms, the simulated IQ phantom was used to assess contrast-to-noise ratios CNR for each hot rod i:

$$\mathrm{CNR}_i = \frac{|\mathrm{I}_i - \mathrm{I}_{\mathrm{ref}}|/(\mathrm{I}_i + \mathrm{I}_{\mathrm{ref}})}{\sigma/\mu}. \quad (1)$$

Here, I_i is the mean intensity of the i^{th} hot rod delineated by the attenuation map, $\mathrm{I}_{\mathrm{ref}}$ is the mean intensity of the reference ROI central to the hot rods (⌀ = 5.4 mm, L = 15.0 mm), and σ and μ are the standard deviation and mean intensity, respectively, in the ROI central to the uniform volume (⌀ = 18.0 mm, L = 11.25 mm). To elaborate, the cylindrical ROIs covered 60% of the active diameter and 75% of the active length based on NEMA's methodology, with the exception of the hot rod ROIs which used the entire diameter and length in analysis. Note that the coefficient of variation CV is represented by the denominator in Eq. 1:

$$\mathrm{CV} = \frac{\sigma}{\mu}. \quad (2)$$

The reconstruction algorithms chosen for comparison of CNR were OSEM, the ordered subsets one step late algorithm with median root prior (OS-OSL-MRP) using a penalization factor of PF = 1.0 **?**, and the ordered subsets separable paraboloidal surrogate algorithm with quadratic prior (OS-SPS-QP) using PF = 0.3 and relaxation parameters of α = 1.0 and γ = 0.1 **?**. The OS-SPS-QP algorithm was initialized with the OSEM image after 21 subiterations.

3.1.4 Resolution in the scatter phantom

To compare resolution with different types of corrections available in the `PinholeSPECTUB` library, the triple line source scatter phantom projection images were reconstructed with the OSEM algorithm in the following configurations: N-C, ATT-C, DOI-C, PSF-C, and ATTDOIPSF-C. In-plane resolution was calculated according to NEMA's methodology from the average full width at half maximum (FWHM) in x and y directions from three 3.5 mm-thick transverse slices: one at the center, and two at $\pm$ 14.5 mm. The average of all x and y FWHM results were then calculated.

3.1.5 Uniformity and variability in the volumetric cylinder

To compare uniformity and variability with different types of corrections available in the `PinholeSPECTUB` library, the volumetric cylinder projection images were also reconstructed with the OSEM algorithm in the following configurations: N-C, ATT-C, DOI-C, PSF-C, and ATTDOIPSF-C. Variability was assessed from the coefficient of variation using Eq. 2, and uniformity U was assessed as

$$\mathrm{U} = \frac{\mathrm{I}_{\mathrm{max}} - \mathrm{I}_{\mathrm{min}}}{\mathrm{I}_{\mathrm{max}} + \mathrm{I}_{\mathrm{min}}} \quad (3)$$

where $\mathrm{I}_{\mathrm{max}}$ and $\mathrm{I}_{\mathrm{min}}$ refer to the maximum and minimum intensities in the ROI central to the uniform volume (⌀ = 15.6 mm, L = 15.75 mm).

3.2 Qualitative assessment of reconstructed *in vivo* data

An *in vivo* dataset was chosen to demonstrate qualitative image quality from an investigation of novel radiotracers for Alzheimer's disease diagnosis **?**. As summarized in Table 2, a B6SJLF1/J mouse was administered an intravenous tail-vein injection with an iodine-123 (^{123}I)-labelled cholinesterase agent with subsequent scan commencing 2 h post-injection. The reconstructed image was visually inspected for uptake in different organs.

Table 2. Summary of *in vivo* acquisition and reconstruction.

Subject	Activity	Acquisition	Projections	Projection matrix	Reconstruction matrix	Algorithm
In vivo mouse	28 MBq	3600 s	91 (7 subsets)	208×208 px, 0.5 mm	230×184×184 vx, 0.25 mm	OSEM

4 RESULTS

4.1 Quantitative assessment of reconstructed data

4.1.1 Computation cost with different matrix corrections

Table 3. Maximum RAM and CPU time required in SPH-SPECT OSEM reconstruction.

	Matrix in memory		Matrix per projection	
Correction type[1]	Max RAM (MB)	CPU time (s)	Max RAM (MB)	CPU time (s)
N-C	4519	57	172	162
ATT-C	4528	227	181	1141
DOI-C	7877	632	225	3484
PSF-C	12025	137	298	422
ATTDOIPSF-C	17012	1417	378	7802
ATTDOIPSFM-C	9875	780	264	4334

[1] N-C: No corrections, ATT-C: Attenuation correction, DOI-C: DOI correction, PSF-C: PSF correction, ATTDOIPSF-C: all corrections, and ATTDOIPSFM-C: All corrections with masking using the default cylindrical mask (⌀ = 34.0 mm).

4.1.2 Contrast-to-noise ratios in the IQ phantom

Figure 3 goes here.

4.1.3 Resolution in the scatter phantom

Figure 3 goes here.

4.1.4 Uniformity and variability in the volumetric cylinder

Figure ?? goes here.

4.2 Qualitative assessment of reconstructed *in vivo* data

Figure 2 goes here.

5 DISCUSSION

6 CONCLUSIONS

CONFLICT OF INTEREST STATEMENT

Dalhousie University and Cubresa share an academic-industry research collaboration.

AUTHOR CONTRIBUTIONS

MS wrote the `ProjMatrixByBinPinholeSPECTUB` class to integrate prototype pinhole-SPECT system matrix estimation software into STIR. MS also performed data collection, image reconstruction, analysis, and wrote the manuscript. CF wrote the prototype pinhole-SPECT system matrix estimation software. All authors contributed to the revision of the manuscript and read and approved the final draft.

FUNDING

This work was supported in part by a Nova Scotia Graduate Scholarship, a series of NSERC grants in collaboration with Cubresa Inc., a CFI grant (37854), and a CIHR grant (PJT- 153319). The software is maintained in part by CCP SyneRBI (EPSRC Grant EP/T026693/1).

ACKNOWLEDGMENTS

The authors would like to thank Drs. Sultan Darvesh, G. Andrew Reid, and Ian Pottie for allowing the acquisition of a single-pinhole SPECT dataset for this study during the investigation of a novel radiotracer for Alzheimer's disease diagnosis as well as Christa Davis for performing the tail-vein injection. The main author would like to thank the Collaborative Computation Project (CCP) for supporting the integration of the software into the open-source STIR framework. The authors would also like to thank Dr. Daniel Deidda for engaging in discussion during the development of the integration software.

DATA AVAILABILITY STATEMENT

The datasets used and/or analyzed during the current study are available from the corresponding author on reasonable request.

FIGURE CAPTIONS

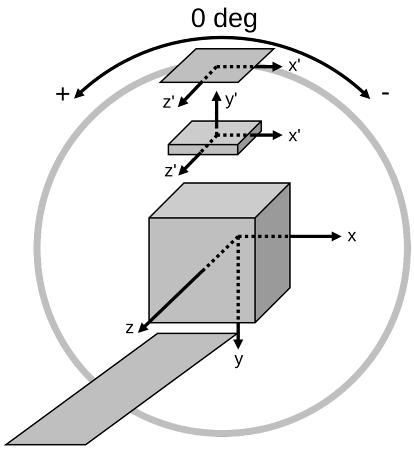

Figure 1. `PinholeSPECTUB` system of reference and sign criteria illustrated for a polygonal collimator setup. Note that the projection matrix adheres to STIR's coordinate system as indicated by the x, y, and z axes. The detector and collimator use a rotating frame of reference where the transaxial x' and axial z' axes coincide with STIR's axes when the detector is at 0 deg. The collimator uses a right-handed coordinate system as indicated by the y' axis which points toward the detector. Further information is given in the text and in STIR's documentation.

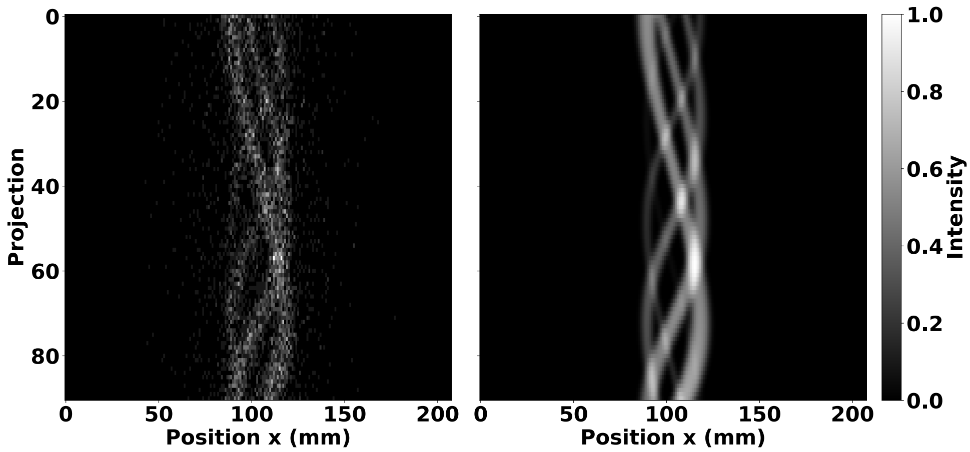

Figure 2. Projection of IQ phantom hot rod region displayed in a 2D sinogram arrangement showing the GATE simulated data (**left**) and the STIR forward projection of the radioactive source distribution adding PSF, DOI, and ATT degradations (**right**).

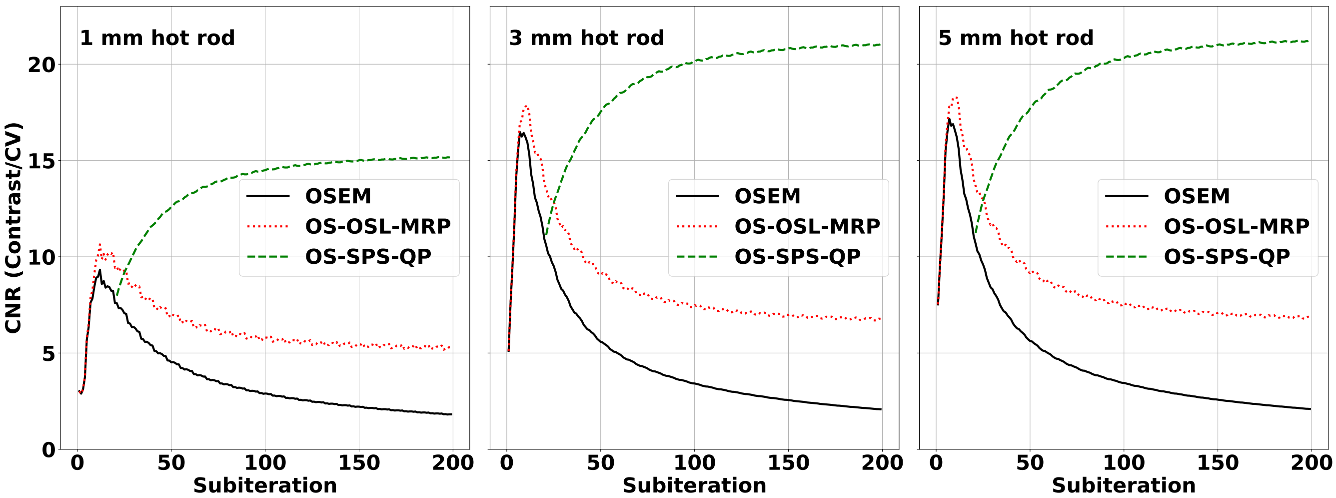

Figure 3. IQ phantom hot rod CNR plots comparing OSEM (solid line), OS-OSL with median root prior (dotted line), and OS-SPS with quadratic prior (dashed line) over subiterations for the 1 mm hot rod (**left**), 3 mm hot rod (**middle**), and 5 mm hot rod (**right**). All images were reconstructed with no matrix corrections and seven subsets, and the OS-SPS-QP reconstruction was initialized using the OSEM image after 21 subiterations. Hot rod contrast was calculated relative to the central inter-rod region void of ^{99m}Tc, and CV was calculated in the uniform ^{99m}Tc region.

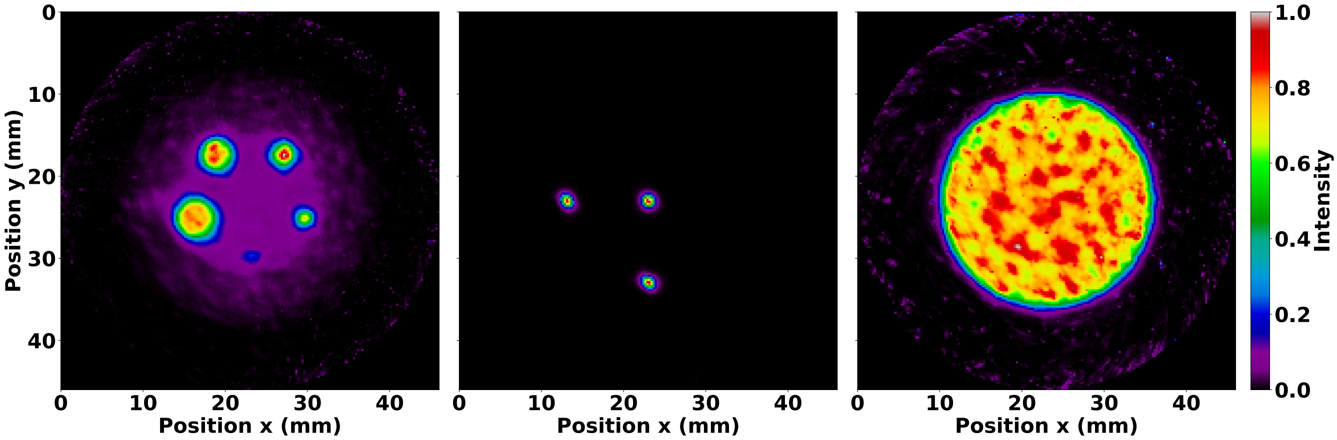

Figure 4. Simulated data. Axial sum of normalized OSEM images after 35 subiterations with no matrix corrections and seven subsets for the IQ phantom hot rods (**left**), mouse-sized NEMA line source phantom (**middle**), and volumetric cylinder (**right**). The IQ phantom image was summed over the length of the hot rods whereas the other images were summed over the entire length of the reconstructed image. Note the expected distributions of ^{99m}Tc.

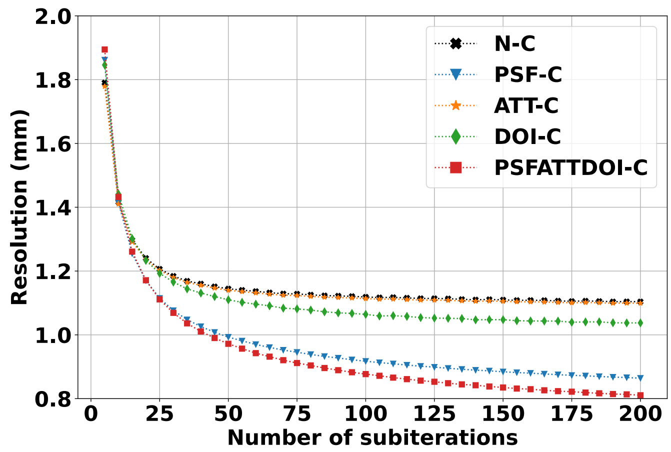

Figure 5. SPECT spatial resolution with scatter in the mouse-sized NEMA triple line source phantom using the OSEM algorithm with seven subsets.

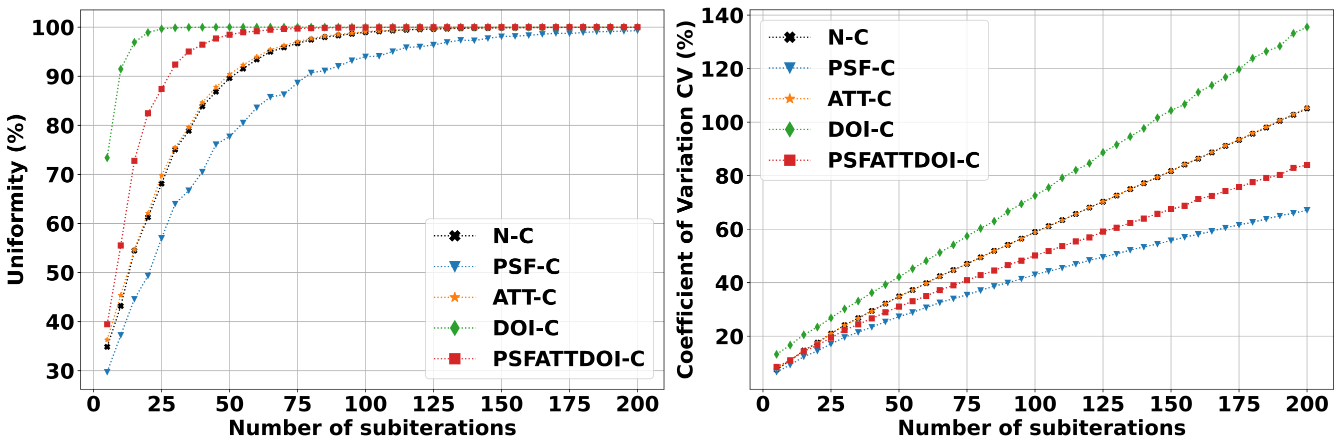

Figure 6. SPECT uniformity (**left**) and variability (**right**) in the volumetric cylinder using the OSEM algorithm with 7 subsets.

Figure 7. Sagittal fused SPECT/CT of the *in vivo* mouse with a window ranging from 0 to 1. The ^{123}I distribution shows a nonpersistent tracer in the brain.

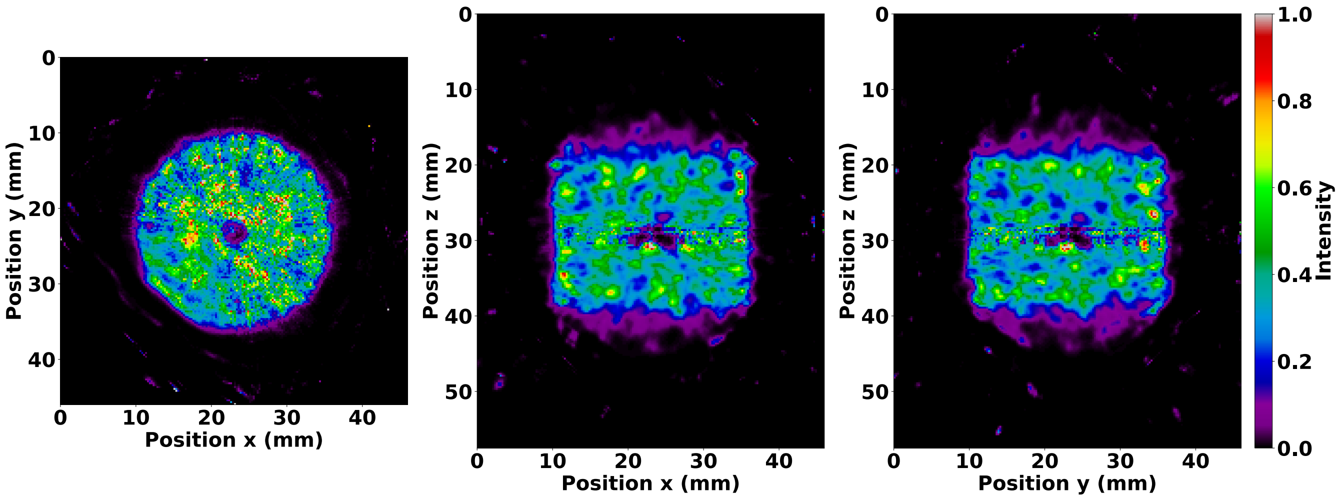

Figure 8. Simulated data. Slices of the volumetric cylinder thresholded between 0 and 1.